The impact of angular momentum on the stellar mass and stellar density of galaxies

Evdokia Kokkinaki

Scholar of the Eugenides Foundation

Division of Astrophysics
Department of Physics

LUND
UNIVERSITY

2024–EXA227

Degree project of 15 higher education credits
June 2024

Supervisors: Corentin Cadiou & Oscar Agertz

Abstract

The current work aims to investigate the impact of angular momentum in galaxy formation especially in the coevolution of the stellar central density ($\Sigma_{\star,1.2\mathrm{kpc}}$) and total stellar mass ($M_\star$). This is achieved by tracing the histories of three simulated halos where the specific angular momentum is altered by modifying the initial conditions of the Lagrangian patch of baryons. The analysis consists of data from a reference galaxy and two cases with increased or decreased angular momentum values for $z = 5$ to $z = 1.95$. The evolutionary trajectories of the given simulations in $\Sigma_{\star,1.2\mathrm{kpc}}$ - $M_\star$ plot are created. The results show that some hints exist about the emergence of a possible pattern between the slopes of the galactic path close to $z = 2$. To detect a clear pattern and thus confirm that angular momentum is the reason that drives this trend, the size of the simulation needs to be expanded to lower redshift values. Additionally, the surface density profile for the three halos at $z = 1.95$ illustrated an indistinguishable behaviour between the corresponding curves, a result that is also reflected in the $\Sigma_{\star,1.2\mathrm{kpc}}$ - $M_\star$ plane. This outcome suggests that despite the notable alternations in the galactic evolution, the central region responds in a similar way until $z = 1.95$.

Galactic Carousel: Does the spin count?

When looking at galaxies through powerful telescopes, one can wonder about their peculiar rotational movements. Do the stars inside galaxies move together like a large carousel? Cosmology attempts to answer this question. Particularly, the structural evolution of galaxies is a significant field of study providing information not only for the current condition of galactic systems but also for their overall evolutionary processes. Recent studies suggest that a potential factor that may affect the formation of galaxies is the angular momentum.

More specifically, the cosmological interpretation of the angular momentum is that of a quantity that provides information about the rotational motion of a celestial object. To visualize the significance of this concept, one can imagine that in the early Universe, the galaxies that we observe now were nothing more than large-scale clouds of gas. If nothing had disturbed the balance of that system these primordial gas clouds would have remained unchanged. However, various events contributed to the change of the Universe's initial conditions, and hence under the influence of the gravitational field, these clouds collapsed inwards. This phenomenon resulted in the cloud being rotated while simultaneously shrinking in size and eventually forming galaxies. Thus the angular momentum enters the equation.

In general, cosmology is a rather challenging field of study as the existing observational instrumentation gives a picture of the present universe at a specific time, making it hard to determine its evolutionary mechanisms. Astronomers use simulations to modify the initial conditions of the early Universe. By analysing the extracted data, hypothetical scenarios can be formed that may lead to potential deductions. A useful tool to create such theories regarding the evolutionary development of galaxies is plotting the total stellar mass against the central stellar density. The method that will be followed in this project to inspect the impact of angular momentum is the creation of such graphs from different values of angular momenta. In doing so, patterns or strong indications of trends showing the impact the angular momentum has on the formation of galaxies will be revealed.

Contents

Chapter 1

Introduction

Angular momentum is a fundamental concept in the field of Astrophysics. Focusing on Cosmology, angular momentum exerts a pivotal influence on processes such as galaxy formation and galactic structural morphology. The specific angular momentum of a rotating object $j_\star$ is defined as the angular momentum per unit mass (Matsumoto 2024). In rotating disks namely, systems where the mass and velocity are not uniformly distributed, the specific angular momentum within radius R can be expressed as follows,

$$j_\star(< R) = \frac{\int_0^R r^2 \Sigma(r) V(r) dr}{2\pi \int_0^R r \Sigma(r) dr},$$

where $\Sigma(r)$ is the surface density and $V(r)$ the rotation velocity (Mancera Piña et al. 2021). A characteristic example of morphological differentiation due to $j_\star$ is between elliptical and spiral galaxies. The former is classified as dispersion-supported cosmic structures with notably low values of $j_\star$ whereas, in the latter $j_\star$ governs both size and orientation of the galactic disk (Cadiou et al. 2022).

In general, galactic angular momentum is contingent upon several factors. Firstly, it is influenced by the initial angular momentum of the early Universe. In fact, early hypotheses state that within a given halo both the gas and the dark matter (DM) components acquire identical spin orientations propelled by tidal torques from the cosmic environment (White 1984). Despite gas cooling during the star formation processes, gas might retain its initial angular momentum, and hence the stellar spin is coupled to the halo spin. Recent research discovers that while $j_\star$ distributions in simulated galaxies and host halos are similar, individual cosmic objects show weak interdependence and notable misalignments (Cadiou et al. 2022).

Another factor that influences the final galactic angular momentum lies in the occurrence of cosmological events that may result in the dissociation of the galactic and the DM halo spins. Such phenomena can be mergers where the angular momentum of the merger alters both the orbital orientation and the magnitude of the host halo spin. Finally, the

proportion of the angular momentum that enters a halo (through gas, for example) and is integrated into the galactic disk influences the final value of $j_\star$. An instance of such a mechanism comes from supernova feedback that is concentrated in the core of the galaxy and may eject low $j_\star$ gas towards the outskirts of the halo, resulting in an augmentation of the disk's spin (Cadiou et al. 2022).

Furthermore, another basic notion that is required for this project is the evolutionary trajectory of galaxies which is discussed in Walters et al. (2021) (henceforth W21). Due to the individual evolution of galaxies, when the stellar mass is held constant the mean galactic size rises as redshift decreases. In addition, a notably stronger correlation is revealed between low levels of stellar formation events (quiescence) and several metrics like diverse size and morphology, than with any other galactic attribute (W21).

The inside-out theory represents the fundamental analytic framework that describes the growth processes of cosmic structures. As the name indicates, galaxies increase their stellar mass from the core and outwards, a phenomenon that is a direct consequence of the top-hat spherical collapse model or TSC (W21). In more detail, TSC characterises the non-linear galactic evolution where spherical collapse and redistribution of angular momentum play a significant role (Kepner 1999; Suto et al. 2016). At the early stages of galaxy formation, both main components, namely, gas and dark matter particles, are coupled and expanding (Kepner 1999). The change of direction of these dark matter shells along with their gravitational collapse lead to the formation of dark matter halos (W21). As the innermost shells collapse at a prior time compared to the outskirts of the halo, lower angular momentum material is located at regions near the core whereas gas with high angular momentum stays outside the galactic bulge (Kepner 1999; W21).

The inside-out progression in galaxy development can be considered a realistic model as several observations and hydrodynamical simulations have confirmed its validity (W21). However, alternative scenarios that contradict the inside-out growth of cosmic structures also exist. One of these deviations is compaction, i.e. events that occur at both high (as initially thought) and lower redshifts and are the result of gas and occasionally star transportation from the outermost regions towards the centre of galaxies due to intense external forces, for example, mergers (Zolotov et al. 2015; W21). These phenomena, caused by mergers or gravitational disturbances in the galactic disk, can trigger bursts of star formation at the core, resulting in a rapid and considerable augmentation of stellar density, with a possible contribution to the bulge. Therefore, the density at the central regions grows, which yields to steeper density profiles and decreases the values for the effective radius. That is why this phenomenon is referred to as compaction (W21).

As previously mentioned, compaction was initially believed to be a process only transpiring at high z. Nevertheless, it is revealed that galaxies with increased central densities are inclined to possess relatively younger innermost regions with concentrated star formation rates (SFRs). Conversely, galaxies characterised by decreased core density exhibit

comparably older centres and have reduced star formation activity (Woo & Ellison 2019; W21). It is consequential to note that the galactic morphology and by extension the core density are not invariably dictated by the angular momentum of the accreting gas (Teklu et al. 2015). According to the classical model of galaxy formation, gas is accreted via two different modes that should have identical values of angular momentum. The cold mode involves dense filaments that do not undergo shock heating and the hot mode that is characterised by radiatively cooling gas from the shock heating of the halo. However, this is not the case as high angular momentum cold gas can be transferred without being mixed to regions with cool angular momentum of the halo gas. Consequently, the angular momentum of the accreting gas is decoupled from the halo. Rather, the most robust correlation with the morphology displayed the alignment between the gas and the angular momentum. The cold filaments of accretion with high angular momentum that are misaligned with the halo (or galaxy at later stages of evolution) contribute to the formation of spheroids. The galactic disk receives substantial contributions from the cooling hot gas of the halo that is characterised by low angular momentum (W21).

Earlier studies have demonstrated that the rate at which the galactic core expands with respect to the overall galactic evolution namely, the evolutionary trajectories in the core stellar density versus total stellar mass diagram, is associated with the specific angular momentum of the accreting gas (W21). In other words, the rate the core increases can be predicted by the total angular momentum of the accreting gas. In Figure 1.1 the histories of 100 isolated star forming (SF) sub-halos at $z = 0$ from the Illustris TNG simulation are depicted. It can be observed that galaxies with dense cores have steeper slopes compared to sub-halos with more diffuse cores that show shallower inclinations. W21 investigates the possible drives behind this behaviour and deduces that the total specific angular momentum of the accreting gas has a strong correlation with the galactic core growth namely, the slopes of the sub-halos in the core stellar density versus total stellar mass plot. More concretely, low angular momentum gas contributes to the growth of the galactic core and high angular momentum gas influences the star formation of the disk. Hence, galaxies that have experienced an inflow of high angular momentum gas tend to undergo evolution with shallower slopes. In contrast, galaxies with low angular momentum illustrate more steep inclinations in central stellar density against total stellar mass plots. Thus, a need exists to examine if $j_\star$ is the reason behind these predictions for simulated galaxies where the angular momentum has been modified. What is the impact of angular momentum on galaxy formation and more particularly on the central stellar density and the stellar mass?

Finally, it is important to briefly highlight the importance of simulations, especially their contribution to our comprehension of galaxy formation. More precisely, the standard dynamical time of galaxy evolution is several million years, a fact that makes direct observation of such phenomena challenging. These observational limitations are overcome by generating galactic simulations and comparing the acquired data with astronomical observations. Moreover, the mechanisms behind galaxy formation and evolution are complex
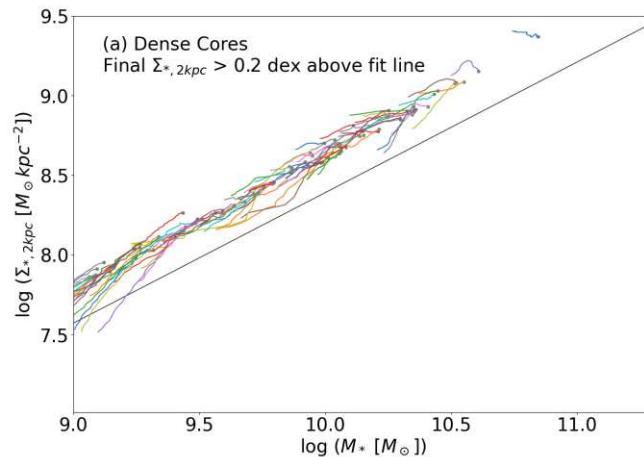
(a) Evolutionary paths for dense cores.
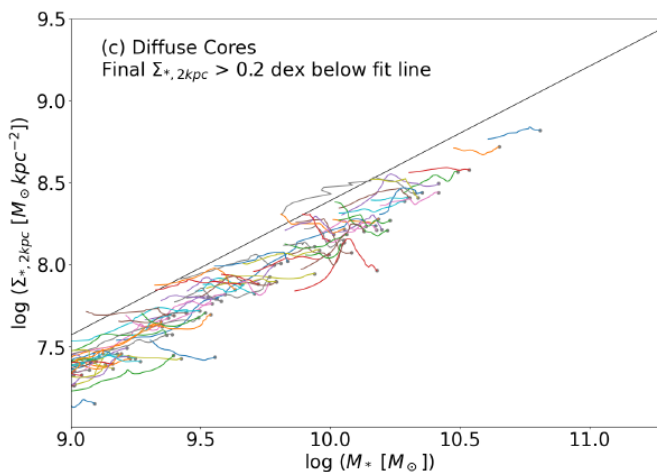
(b) Evolutionary paths for diffuse cores.

Figure 1.1: Plots depicting the coevolution of central stellar density $\Sigma_{\star,2\text{kpc}}$ and the total stellar mass $M_\star$ in the Illustris TNG simulation (W21). It focuses on tracing the history of 100 isolated SF (star forming) sub-halos with shallow and dense cores at $z = 0$. A trend regarding the slopes of the evolutionary paths is extracted from these plots, namely galaxies with dense cores (sub-figure (a)) have steeper slopes, whereas sub-halos with diffuse central regions develop a shallower inclinations (sub-figure (b)). The solid line is the least squares fit with face-on values (observations viewed from above the plane of the galaxy, opposed to edge-on values) for the core density $\Sigma_{\star,2\text{kpc}}$. W21 investigates the possible drivers behind this behaviour, and argues that galaxies with high angular momentum infalling gas show shallow slopes in $\Sigma_{\star,2\text{kpc}}$ - $M_\star$ and gas with low angular momentum results in steeper slopes. These plots has been used several times throughout this project, as it illustrates the expected trend in $\Sigma_{\star,2\text{kpc}}$ - $M_\star$.

and involve a significant number of parameters. Simulations on the other hand permit the modification of galactic systems into different scenarios that incorporate the appropriate at-the-time processes such as star formation, gravity, supernovae and black hole feedback, and angular momentum alternations.

Focusing on the objective of the current work, the accuracy and validity of theoretical models that describe the galactic formation and evolution processes can also be tested through simulations. Existing theoretical frameworks can be enriched and refined by weighing the simulation data against the observational ones. More specifically, it has been indicated that keeping the mass constant, galaxies with low $j_\star$ are more compact with a significant bulge and decreased galactic disk. In contrast, halos with increased angular momentum are more elongated in space and possess a more definite and notable disk with a smaller bulge (Cadiou et al. 2022). Therefore, another broad question that this project can potentially contribute to answering is the reason that these distinct types of galaxies exist.

Although simulations are invaluable tools, recognising and addressing the possible caveats associated with each model, like resolution limitations and initial assumptions that can affect the interpretation of the results, is a crucial part of the research procedure. A significant caveat originates from the redistribution of angular momentum of the gas in galaxy disks that consist of stars. This rearrangement is a key function in understanding disk instabilities such as spiral arms and pseudobulges (Sellwood 2014). Gas turbulence can alter the distribution of angular momentum too, impacting both the morphology and dynamics of the disk (Forbes et al. 2014).

The structure of this project is as follows. First, the methodology is described including a description of the galaxy simulations in Chapter 2. Then, in Chapter 3 the results are presented and analysed in a comprehensible way along with the corresponding plots. Finally, the implications of our results are discussed in Chapter 4.

Chapter 2

Methodology

2.1 The Simulations

To research and analyse the scientific question posed in Chapter 1, it is crucial to comprehend the mechanisms behind the three simulations the data are extracted from. The first step is to create the hydrodynamic zoom simulations for the reference galaxies. Starting from the production of the initial cosmological conditions using the GenetIC approach (Stopyra et al. 2021) a 512^3 dark matter-only simulation within a cosmological box of co-moving side length $100 \ \mathrm{h}^{-1} \cdot \mathrm{Mpc}$ is created. As massive galaxies of mass within the virial radius $M_{\mathrm{vir}} \approx 10^{12} \ M_\odot$ and at redshift 2 exhibit diverse structural morphologies, three halos (A, B, and C) are arbitrarily chosen for subsequent resimulation at high resolution (Cadiou et al. 2022). The viral radius (R_{vir}) is a characteristic radius that is used to specify the boundaries within which the mass of a galaxy is in virial equilibrium. According to the virial theorem, R_{vir} refers to a region at which the total kinetic energy of a self-gravitating, stable, and spherically symmetric system is equal to $-1/2$ the total gravitational energy (Carroll & Ostlie 1996).

These three halos are characterised by the absence of any significant merger between redshifts 2.5 and 2, as well as the lack of any massive neighbouring cosmic structures within a 500 kpc distance, for the low-resolution DM-only simulation. In contrast, for high-resolution methods, initially unresolved mergers can be detected. More precisely, 1:5 mass ratio mergers are observed in $z = 2.3$ and $z = 2.2$ for halos A and B, and a 1:6 merger event occurred at $z = 2.3$ for halo C. The Lagrangian patch of particles with a range of three virial radii is found for the three halos to occupy with high-resolution dark matter particles the corresponding regions during the early Universe epoch (Cadiou et al. 2022). The Lagrangian patch is a fundamental component in dissecting the evolution and distribution of baryons in the simulated halos. It is characterised by particles in the initial cosmological conditions that will form a distinct structure (galaxies or dark matter halos) due to their gravitational collapse. In simulations, Lagrangian patches are used to find and trace specific regions of space that will eventually evolve into denser regions (Bernardini et al. 2020).

The obtained hydrodynamic simulation of the reference galaxy is resimulated for different values of angular momentum using a combination of the genetic modification method (Roth et al. 2016) developed to alter the initial angular momentum of the early Universe (Cadiou et al. 2021) for a specific region. Minimal systematic alternations of the initial density field achieve this. Inducing a 'spin-up' effect by introducing minor overdensity along the leading boundary of a large patch and the equivalent underdensity on the trailing edge are instances of such adjustments to the initial conditions. These modifications are intentionally small to preserve the large-scale environment as unaffected as feasible (Cadiou et al. 2021, 2022).

To start altering the angular momentum, the first step is to specify an appropriate region of the reference halo during the primary stages of the Universe. At redshift 2, the central galaxy is identified along with the necessary tracer particles namely, stars, gas, and those associated with accretion onto supermassive black holes, within an area four times the half-mass radius ($R_{1/2}$). We define $R_{1/2}$ as the radius of the galaxy that corresponds to half the total stellar mass enclosed within the virial radius $M_\star(< R_{\mathrm{vir}})$. Subsequently, the baryonic Lagrangian patch of the reference simulation is established by conducting a reverse tracing of the baryons at $z = 200$. Implementing the genetic modification method to the Lagrangian patch of baryons during the initial cosmological conditions for the reference galaxy, the supplementary simulations where the angular momentum has been altered are generated (Cadiou et al. 2022).

Four distinct galactic initial conditions where a specific factor has adjusted the stellar angular momentum are considered to ensure that the results address a broad range of angular momentum cases. These amplitudes are $\times 0.66$, $\times 0.80$, $\times 1.2$, and $\times 1.5$ relative to the stellar angular momentum of the reference simulation. An additional reason for selecting these values of $j_\star$ is because it permits control over the angular momentum during the evolution of the galaxy, compared to the angular momentum of the dark matter j_{DM} and baryons j_b. Particles in the outermost regions dominate the angular momentum of the simulated halo. Hence, any such perturbations can have a notable impact on j_{DM} and j_b. Yet, any alternations in the halos' edge have minimal influence on $j_\star$, as stars occupy the innermost regions of the gravitational potential (Cadiou et al. 2022).

By modifying the initial conditions of a specific region for the reference halo, the time at which the major mergers occurred close to $z = 2$ is either delayed or hastened. The reason for this phenomenon lies in the fact that the fluctuations in angular momentum affect the orbital trajectories of the satellite galaxies even when they are located within the R_{vir}. The differences in values for the central galaxy mass compared to the dark matter and stellar mass ones are proof of that (Cadiou et al. 2022). As a consequence, various simulations with distinguishable amplitudes of stellar angular momenta at redshift 2 are created, with their final $j_\star$ value to be either reduced or increased when juxtaposed with the reference case.

In total, the numerical experiment described above resulted in fourteen simulations, from which three of them are the reference galaxies for halos A, B, C and the rest correspond to the four alternating scenarios of angular momentum. The case of $\times 1.5$ for halo C is omitted as the time the satellite falls in the galaxy takes place after the simulation is concluded due to a large delay. For each simulation, the mass of the stellar particles enclosed in the virial radius is $\sim 10^{11}$ $M_\odot$ and the dark matter mass is $\sim 10^{12}$ $M_\odot$ (Cadiou et al. 2022). In the current work, the cases of 0.66, 1.2, and the reference one were studied in detail. The case of 1.5 was also examined. However, the latter case is omitted from the final evaluation since its assembly is significantly delayed due to a major merger at $z = 2$ (Cadiou et al. 2022). This will be further discussed in Chapter 3.

To generate the aforementioned simulations the mesh refinement code RAMSES (Teyssier 2002) has been used, incorporating gravitational softening of 35 pc and a minimum cell size along with dark matter mass resolution of $M_{\mathrm{DM}} = 1.4 \cdot 10^6$ $M_\odot$ and stellar mass resolution of $M_\star = 1.1 \cdot 10^4$ $M_\odot$ (Cadiou et al. 2022). In cosmology simulations, gravitational softening is applied to avoid numerical inaccuracies caused by extreme gravitational interactions between closely situated particles or cells. This technique is used to define the minimum distance over which gravitational forces are estimated accurately. In the aforementioned simulations, the gravitational interactions between cells or particles are softened over distances larger than 35 pc (Aarseth 2003). The numerical experiments are conducted within a cosmological framework described by a dark energy density of $\Omega_\Lambda = 0.69$, a total mass density of $\Omega_m = 0.309$, a Hubble constant of $h_0 = 67.7$ km s^{-1} Mpc^{-1}, and a mass density of baryons $\Omega_b = 0.0486$ (Cadiou et al. 2022).

The NewHorizon (Dubois et al. 2021) method is used to incorporate sub-grid baryonic physics which allows star formation above a gas density threshold of $n_0 = 10$cm^{-3} from Schmidt law. The usage of this simulation technique results in more compact galaxies, a fact that impacts the selection of a proper radial distance for the calculation of the core density as it will be explained in Chapter 3. Moreover, to model the stellar populations the Kroupa (2001) initial mass function is implemented which in brief specifies the distribution of masses for a stellar population during star formation. Additionally, regarding supernovae, it is assumed that the proportion of the stellar mass that is ejected into space during the explosion is $\eta_{\mathrm{SN}} = 32\%$ and the amount of heavy metals that are included in the erupted material or metal yield is 0.005. In the simulations, type II supernovae are also considered through the utilisation of a specific mechanical feedback model that describes the dynamics of such explosions. Finally, the processes associated with the formation and evolution of supermassive black holes are also included, by integrating their energy release via active galactic nucleus (AGN) feedback mechanisms (Cadiou et al. 2022).

2.2   Initial method: DM centring

As it was previously noted, data from three simulations are investigated along with an additional simulation of the ×1.5 case for halo A. To conduct this analysis four different `.csv` files are supplied, one for each simulation, that contains the position of the main galaxy as a function of time. More specifically, the time in Gyr, the virial radius in physical kpc, the (x, y, z) coordinates in comoving kpc, and the corresponding (x, y, z) unitary coordinates in comoving box units, i.e. values between 0 and 1, are included in each row of the `.csv` file. It is worth mentioning that the difference between the physical and the comoving units is that the latter takes into account the expansion of the Universe (Hogg 1999). As it will be thoroughly explained the provided positions of the galaxies are estimated centring on DM, a fact that will create an offset in the calculations. The raw data from the simulations are grouped in folders incorporating snapshots of the simulated Universe (outputs) at specific redshifts for each galaxy; from $z = 5$ to $z = 1.95$ for the reference galaxy (14 outputs), from $z = 3.6$ to $z = 1.94$ for the ×1.5 case (8 outputs), from $z = 3.9$ to $z = 1.94$ for the ×1.2 galaxy (9 outputs), and for $z = 3.6$ to $z = 1.94$ for the ×0.66 simulation (8 outputs). In total, the necessary space required to perform this data analysis is 1TB and for that reason, access to a server is given through an SSH tunnel.

The analysis is executed in Jupyter Notebook (Kluyver et al. 2016) utilising several libraries to load, study, and visualise the data. More specifically, the Python-based `yt project` (Turk et al. 2011) is mainly used to load the simulation data, perform the necessary data analyses, and generate high-quality visualizations such as particle plots. Also, `pandas` (Wes McKinney 2010) are used in the data analysis to read the `.csv` files that contain the relevant information and `matplotlib.pyplot` (Hunter 2007) is preferred for the customisation of plots.

This project focuses on the correlation between the evolution of the central core density for the given simulations with respect to the total stellar mass. The central density is commonly quantified as the surface density of the stellar mass within a predetermined radial distance r in spherical coordinates, as W21 states. It can be denoted as $\Sigma_{\star,r}$ and characterises how compact the central region of a galaxy is. It is significant to acknowledge that $\Sigma_{\star,r}$ is not the true surface density of the galaxies. W21 argues about the importance of using face-on projected values while tracing the histories of the halos. With face-on values, i.e. the observational perspective that views a galaxy form a position perpendicular to its plane, a consistent reference frame is established as allows our observations to be aligned with the halo's rotation plane. Let $M(< r)$ be the stellar mass enclosed within a sphere of radius r, then the surface central density is defined as follows,

$$\Sigma_{\star,r} = \frac{M(< r)}{\pi \cdot r^2} \ . \tag{2.1}$$

The initial approach is to create a function which takes into account the raw data and the position of each simulated galaxy and through the definition of two concentric spheres

with different radii (the virial radius and fixed radius r for $\Sigma_{\star,r}$) the core density can be computed. Additionally, using the appropriate fields from the yt (Turk et al. 2011) the stellar mass within the spheres is found and then converted to $M_\odot$. The function (process()) is as follows,

```
def process(ds, row, rad):
    center = [row.x_unitary, row.y_unitary, row.z_unitary]
    virial_radius = ds.quan(row.virial_radius, "kpc")
    region = ds.sphere(center, 0.2 * virial_radius)
    inner_region = ds.sphere(center, rad)

    stellar_mass = region[("star", "particle_mass")].sum().to("Msun")
    inner_mass = inner_region[("star", "particle_mass")].sum().to("Msun")

    core_density = inner_mass / (np.pi * (rad ** 2))
    return stellar_mass, core_density
```

In more detail, process() considers three parameters: ds representing the cosmological dataset containing relevant information about the galaxy, row which included the positions of the galaxies as a function of time, and rad denoting the radius r of the inner region of interest within the galaxy for $\Sigma_{\star,r}$.

This function extracts the spatial coordinates of the galaxy's centre from the row object and encapsulates them within a list named centre. Subsequently, the virial radius of the galaxy is converted into kpc. This parameter is crucial for defining spatial regions within the galaxy for subsequent analysis. Then, the process function defines two distinct spherical regions within the galaxy utilizing the sphere method provided by the ds argument. The first region represents a spherical volume centred at the previously extracted coordinates with a radius equivalent to 20% of the virial radius. This choice of radius enables the focus on a substantial portion of the halo. The second region, denoted as inner_region, is centred at the same coordinates but possesses a radius specified by the rad parameter, facilitating analysis within a more confined spatial extent.

Following region definitions, process() calculates the total mass of the stellar particles within each spherical region, by summing the masses of these particles residing within the respective regions. Particularly, stellar_mass represents the total stellar mass within the 20% of the virial radius, while inner_mass quantifies the total stellar mass within the specified inner region. In addition, the function calculates the core density $\Sigma_{\star,r}$, a significant metric for this project as it characterises the distribution of stars within the galaxy's central regions. From equation 2.1 the calculation involves dividing the stellar mass within the inner region by the area of the circular cross-section defined by the inner region's radius. Conclusively, the function returns the two key quantities namely, the stellar_mass, signifying the total stellar mass enclosed within the 20% of the virial radius, and core_density,

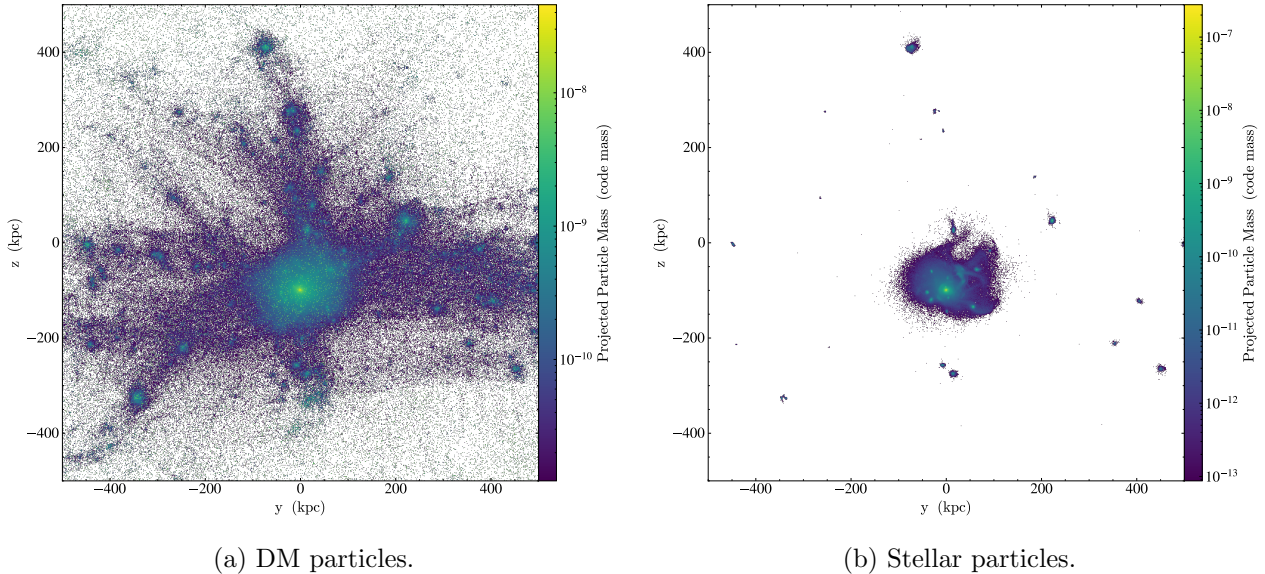(a) DM particles.   (b) Stellar particles.

Figure 2.1: Projection plots illustrating the dark matter particles (a), and the stellar particle distribution (b) in the reference galaxy at $z = 1.95$. For comparison reason, sub-figures (a), (b) have the same size of 100 kpc. As the region incorporating DM particles is notably more extended than focusing on stars, the centring method used in the analysis is refined.

signifying the central stellar density $\Sigma_{\star,r}$. The evolutionary tracks of the simulated galaxies are generated by plotting $\Sigma_{\star,r}$ for a specific radial distance r against the stellar mass $M_\star$.

2.3 Shrinking Sphere method

As previously stated, the given positions of each galaxy as a function of time are approximated by utilising dark matter particles. Hence, both regions in `process()` are centred on DM particles instead of stars, a fact that results in a significant offset in the produced $\log(\Sigma_{\star,r})$ - $\log(M_\star)$ plane. This discrepancy is illustrated by notably decreased values of $\Sigma_{\star,r}$ (dips) at certain redshifts, as can be seen in Figure 3.3 (a). Therefore, the need to modify the `process()` function so that the regions used to compute the core density of each snapshot are centred on stars instead of dark matter arose. This is achieved by the shrinking sphere method (Power et al. 2003), which involves the iterative computing of the centre of mass of stellar particles within a shrinking sphere until the number of star particles contained within the sphere is reduced to the predetermined threshold of 1000 particles.

More concretely, the procedure starts with a large sphere that encompasses a large fraction of the galactic system, i.e. the spherical regions as initially defined in `process()`. The initial sphere's centre is then recalculated as the centre of mass of the stellar particles within

the spherical region, and the sphere's radius is reduced by a certain percentage namely, 5%. This process is iteratively repeated until the specified threshold of 1000 stellar particles within the high-resolution region is reached within the sphere. The resulting centre obtained from this method is used as the centres of each halo which are independent of the initial parameters centred on dark matter particles and hence, it provides more accurate halo centring, especially for spherical asymmetric galaxies (Power et al. 2003). It is significant to note that converting the aforementioned values to the appropriate units for the analysis was a key issue for this step.

The code that describes the aforementioned technique will be explained in detail and is given in the Appendix. The key parameters that are needed for the `shrinking_sphere()` function are: `ds` denoting the dataset, `centre` and `radius` representing the initial centre and radius of the spherical regions, `center_on` that specifies the type of particles to centre on i.e. stellar particles, and `shrink_factor` that establishes the factor by which the radius of the sphere is reduced after each iteration. In the present case, the radius is shrunk by 5%.

In more detail, several steps needed to be followed to acquire new and more accurate centres. First and foremost, the function performed the necessary data preparation by excerpting the coordinates for both the initial centre and the virial radius of the halo as it is provided from the `ds` dataset. As these values are in the form of tuples they are converted to the desired units. Utilising the aforementioned values, a spherical region `sp0` is generated and the positions `pos` and masses `m` for the enclosed particles are attained. Then, the shrinking loop of the function begins under the requirement that the number of enclosed stellar particles `len(pos)` is decreased to 1000 or fewer. For each iteration of the loop, two quantities are logged namely, the current radius of the sphere along with the number of stellar particles. The value of the radius is evaluated as the distance between the current centre and the initial centre (`center_0`). Additionally, using the positions of the particles in the region, the function provided the Euclidean between these particles and the current centre.

The `np.linalg.norm` function is used to compute the magnitude of the Euclidean distance along the specified axis. The command `axis=1` ensures that the norm is calculated relative to rows. The order of the particle indices, which depends on their corresponding distances from the centre, is returned by `np.argsort(r)`. Furthermore, the code snippet `new_len = min(int(len(pos) * shrink_factor), len(pos) - 1)` indicates the newly acquired length of the stellar particle array `pos` after the converging requirement of the `shrink_factor` is met. In other words, the new length contains the stellar particles closest to the centre of the sphere after the radius has been decreased by 5%. Also, to guarantee that the length of the particle arry is not reduced below the threshold of `len(pos) - 1` the `min` function is utilised. Then, the particle array is redefined to sort through the subset of particles closest to the centre as determined from the new length, using the relevant indices (`order`). Lastly, the new centre of mass is extracted by estimating the weighted av-
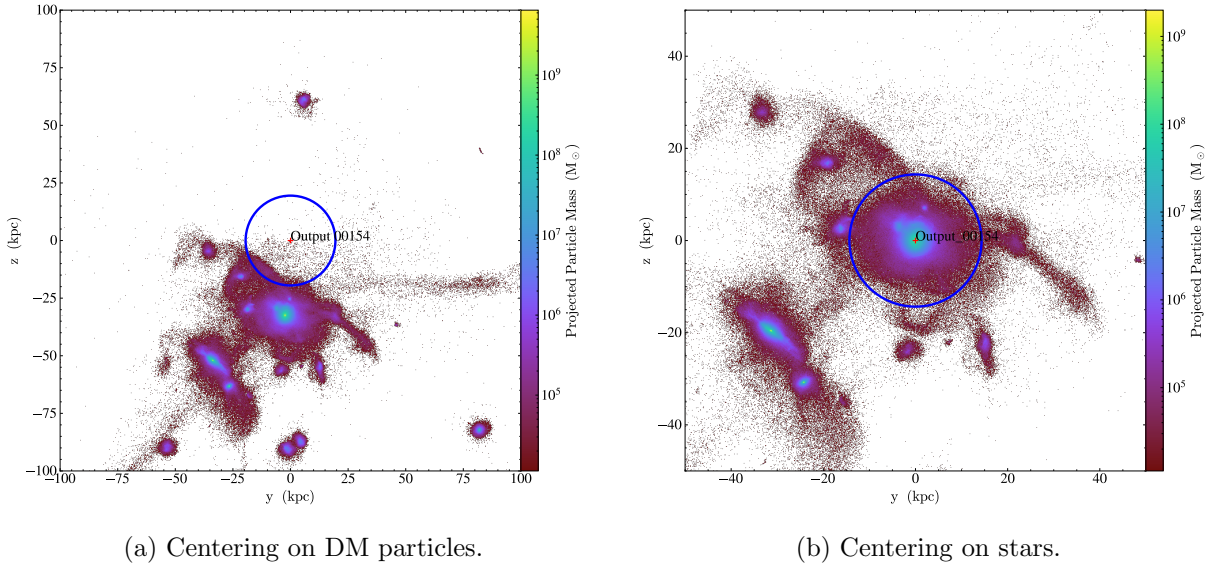
(a) Centering on DM particles.   (b) Centering on stars.

Figure 2.2: Comparison between the two centres for the ×0.66 simulation at redshift 2.5. In the initial approach when the centres of the spherical regions are relative to DM (left) it is illustrated that there is a significant offset. In contrast, by redefining the central point on stellar particles (right) this discrepancy is eliminated and hence the values of core density can be calculated.

erage of stellar particle positions `pos` from their masses `m`. The new centre of the spherical region is deduced as the weighted average is calculated along the specified axis of `axis = 0`.

After redefining the centres for the utilised spherical regions in the `process()` function, it is crucial to inspect if the centering is indeed more accurate. An efficient method to achieve that is to create particle plots for each given snapshot of the galaxies from the `yt` (Turk et al. 2011) library and visually check the position of the new spherical regions centring on stars. To be specific, the generated particle plots illustrate the spatial distribution of stellar particles along the y and z axis (`("star", "particle_position_y")`,`("star", "particle_position_z")`). Moreover, they incorporate information regarding the stellar mass of each particle in the simulated galaxies (`("star", "particle_mass")`). Through the illustration of the stellar particles' mass, it becomes visually possible to identify regions with diverse stellar densities contained in the halo. The plots can be centred around either the new central points acquired from the `shrinking_sphere()` method or the initial centres. Finally, the size of the region displayed in the particle plots is determined by the width parameter which in our case is 200 kpc, as can observed in the code below.

```
particle_plot= yt.ParticlePlot(ds, ("star", "particle_position_y"),
                ("star", "particle_position_z"),
                ("star", "particle_mass"),
                center=center, width=(200,"kpc"))
```

In sub-figures 2.1(a) and (b) where the dark matter and the stellar particle plots of the reference galaxy at $z = 1.95$ are displayed, the impact on centring in DM particles instead of stars can also be seen. The spatial distribution of DM is significantly extended compared to stellar particles. Hence a region that is well-centered in the DM case, could not be an appropriate one in the stellar particle case.

As it will be further rationalised in Chapter 3, the centring problem is resolved by the new centres and thus the evolutionary trajectories of the simulated galaxies can be computed. The particle plots in Figure 2.2 illustrate an instance where the contrast in centring between the initial and the new method is considerable. In these plots, the centres along with the region that represents the 20% of the $\times 0.66$ galactic simulation are annotated at $z = 2.5$. Additionally, the particle plots will be used to visually identify the major merger event for each simulation that is crucial in order to confirm or infirm if the evolutionary process in the $\Sigma_{\star, 1.2kpc}$ - $M_{\star}$ plane are driven by the angular momentum.

Chapter 3

Results

The current work aims to investigate the effect of angular momentum on the stellar formation and evolution of galaxies. This is achieved primarily by two steps. Firstly, the evolutionary trajectories of the same galaxy with three different values of angular momenta are obtained, and then a possible pattern between these tracks is identified to determine the impact of angular momentum on the stellar mass and stellar surface density. In other words, the evolutionary paths of the corresponding subhaloes are documented by tracking their core growth through the $\log(\Sigma_{\star,1.2\text{kpc}})$ - $\log(M_\star)$ plane like it was done in W21. Afterwards, depending on the difference in slopes these three paths have at redshift 2 and 1.95, the influence of angular momentum in stellar formation can be distinguished.

3.1 Selection of radius

In W21 the central stellar surface density is computed by selecting a spherical region with a fixed radius r in kpc. Therefore, it is necessary to ascertain a specific range of values for r in which any emerging pattern between the tracks can be determined. To achieve this, the surface density profile of the galaxy at redshift 1.95 is investigated. In more detail, the logarithmic values of the core density $\Sigma_{\star,r}$ are plotted as a function of radial distance r from very small values till 2 kpc which is the effective radius in W21 (Figure 3.1). Ideally, the surface density profile would provide the proper radius r for which the expected trend in the evolutionary trajectories for the different occasions of $j_\star$ would be visible. However, that is not the case as the curves are indistinguishable from each other, as can be seen in Figure 3.1. Hence, the selection of the appropriate fixed radius for $\Sigma_{\star,r}$ needs to be deduced using different criteria.

In parallel, cross-checking the acquired surface stellar density $\Sigma_{\star,r}$ with the corresponding values from the simulation in Cadiou et al. (2022) is a necessity for this project. This comparison is attained utilising the given values for the total stellar mass and the effective radius R_{eff} of halo A for the three relevant simulations (Cadiou et al. 2022). The calculated R_{eff} is the half-mass radius $R_{1/2}$. Thus, the expression that describes the stellar mass

contained in $R_{1/2}$ is as follows,

$$M_\star(R_{1/2}) = \frac{M_\star(< R_{\mathrm{vir}})}{2} \, . \tag{3.1}$$

Implementing the equation 3.1 to the total stellar mass values for each simulation, $M_\star(R_{1/2})$ is attained. Then, substituting the aforementioned mass to equation 2.1 along with the effective radius R_{eff}, the values for the core density $\Sigma_{\star,R_{\mathrm{eff}}}$ are computed. In Table 1 the logarithmic values for this density are listed with reference to the which $j_\star$ case they correspond to. These points are annotated in Figure 3.1 for visual reference.

From the surface density profile (Figure 3.1) it is clear that there exists a small offset between the previously calculated values and the corresponding points in the plotted curves. The reasons behind this inconsistency are unclear. One possible explanation could be that the obtained stellar mass is taking into account the extra mass that is added to the galactic system after the satellites have been merged whereas, the analogous $\Sigma_{\star,R_{\mathrm{eff}}}$ points are estimated by using the values for stellar mass not considering the contribution of the major merger for each halo. Yet, it is understood that this cannot be the only justification as diminishing the stellar mass will result in more reduced $\Sigma_{\star,R_{\mathrm{eff}}}$ values compared to the estimated ones. Nevertheless, identifying the cause is a rather complex problem that requires further investigation which is beyond the scope of this project. Despite this deviation, the three curves are still indistinguishable from each other and a conclusion regarding the selection of the appropriate fixed radius cannot be deduced from this method.

An additional way to qualitatively evaluate the results obtained from our analysis is to estimate the half-mass radii $R_{1/2}$ at $z = 1.95$ and compared them with the corresponding tabulated ones denoted as R_{eff} in Cadiou et al. (2022). To find these values the stellar mass profile of each galaxy is created. More concretely, the total stellar mass within the virial radius of each simulation is plotted as a function of radial distance as shown in Figure 3.2. Then the point of the resulting curve that corresponds to the radius at which the galaxy obtains half its total stellar mass namely, $R_{1/2}$ is approximated and recorded in Table 2. Comparing the acquired values with the relevant R_{eff} it is noted that there are not identical and a discrepancy between them exists; 0.18 kpc for the ×0.66 case, 0.71 kpc for the reference galaxy, and 0.83 kpc for the ×1.2 simulation. As previously mentioned one possible justification that can explain this deviation in values could be that in this work, the extra stellar mass that is added to the system from infall satellites is considered in the calculation. However, the source of this divergence is not obvious and requires further analysis which is beyond the scope of this project.

Nevertheless, by studying the produced stellar mass profiles a better understanding of the different evolutionary processes that occur during the simulations is achieved. In more detail, as it can be remarked from Figure 3.2 the evolution of the total stellar mass can be distinguished into three main phases. During the early stages of galaxy formation, there is a dramatic increase in stellar mass, an observation that is confirmed by the corresponding
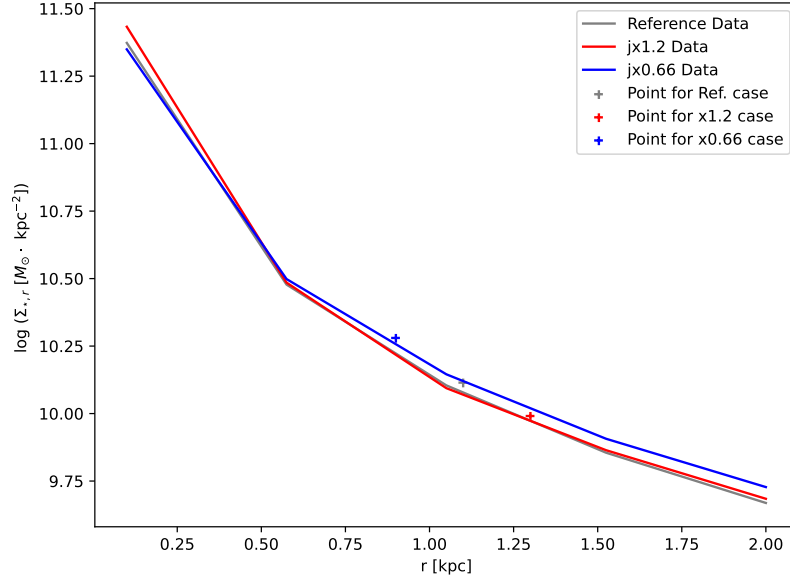
Figure 3.1: Surface density profile for the three different cases of stellar angular momentum at $z = 1.95$. In order to discern between the different values of the angular momenta, the curves are coloured (red for the $\times 1.2$ case, blue for the $\times 0.66$ case, and grey for the reference case). For visible reference, the corresponding values of the central stellar surface density $\Sigma_{\star,R_{\mathrm{eff}}}$ as they have been computed using the given stellar mass and effective radius from Cadiou et al. (2022) are annotated.

particle plots for high redshifts. As the radius increases this rapid growth rate of $M_{\star}$ is reduced until a certain value of r where the curve demonstrates a plateau-like behaviour. In this part of the diagram, the galactic stellar mass exhibits a minimal to almost non-existent increase, a phenomenon that is also verified visually in the particle plots for the relevant z. The last part of the curve represents the time when the major satellite merges with the central galaxy and hence the illustrated slight augmentation of $M_{\star}$. This merger event happens when the satellite is within the virial radius and is situated in the outermost regions of each galaxy. As explained in Chapter 2 this is a crucial incidence for our analysis since the modifications in angular momentum occur through these mergers. Figure 3.2 (a) shows the mass distribution of the $\times 0.66$ simulation at $z = 1.95$ and in Figure 3.2 (b) the stellar mass profile of the reference galaxy at $z = 2.4$ is depicted. In the latter case, the stellar mass distribution is notably different from the former case because at approximately $z = 2.4$ the satellite of 1:3 mass ratio crosses the R_{vir} and merges with the primary galaxy. Hence the dissimilar profiles.

An alternative approach in identifying the most efficient fixed radius for the central density $\Sigma_{\star,r}$ is to consider the effective radius of the simulated galaxy for the three different in-
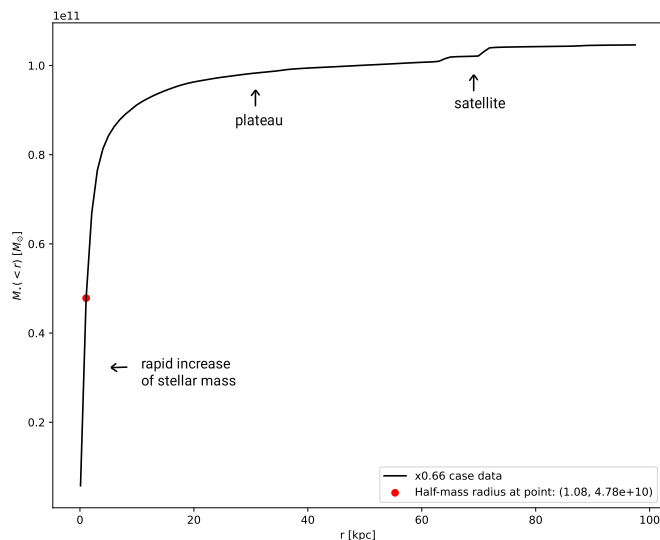
(a) Stellar mass profile for the ×0.66 case at redshift 1.95.
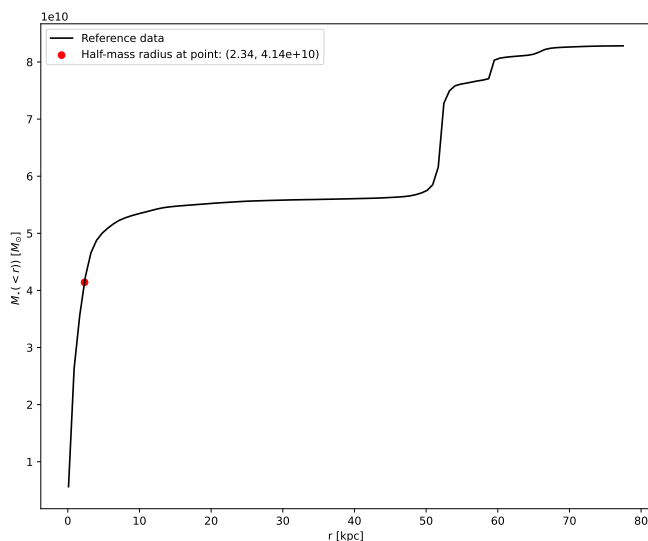
(b) Stellar mass profile for the reference case at redshift 2.4.

Figure 3.2: Graphs depicting the stellar mass profiles of the ×0.66 simulation (left) at $z = 1.95$ and the reference galaxy (right) at $z = 2.4$. Plotting the total stellar mass as a function of radial distance contributes to understanding the evolution processes that occurred in the simulations. In sub-figure (a), the three main phases of the mass distribution are annotated. First, there is a rabid mass increase during the early stages of the galaxy formation, which is gradually reduced into the plateau part of the graph for higher z. Finally, towards the end of the simulation, the satellite merged with the main galaxy hence a small increase in the stellar mass. A more notable merger event is depicted in sub-figure (b) at redshift 2.4.

stances of angular momentum and choose r to be within the range of this R_{eff} values. The rationale behind this decision originates from the fact that in galactic structures undergoing star formation the core density $\Sigma_{\star,r}$ exhibits a robust correlation with the effective radius (W21). Therefore, it can be deduced that the selection of a suitable radial distance r when computing the defined core density $\Sigma_{\star,r}$ is a key point for this analysis. As it was previously mentioned, specifying the surface central density $\Sigma_{\star,r}$ within the range of the effective radius is the most efficient procedure so as to recognise possible patterns that indicate the impact changes in angular momentum have in galaxy formation. Thus, the radial distance of $r = 1.2$ kpc ($\Sigma_{\star,1.2\text{kpc}}$) is chosen as it is in the range of the half-mass radii for the three different cases of $j_{\star}$ that are going to be studied.

The fact that the simulated zoomed-in galaxies are denser can further justify the selection of $\Sigma_{\star,1.2kpc}$. In more detail, the three different simulations are attained using the NewHorizon model (Dubois et al. 2021) which compared to observations creates massive galaxies that are more compact. It is also true that at redshift 2.0 galaxies are more compact by a factor of approximately two than at redshift $z = 0$ (Swinbank et al. 2017). As in W21 a radius of 2 kpc is used instead of 1.2 kpc ($\Sigma_{\star,2\text{kpc}}$) to attain the Illustris TNG subhalo histories in the $\Sigma_{\star,2\text{kpc}}$ - $M_{\star}$ plane, the evolutionary trajectories in the $\Sigma_{\star,2\text{kpc}}$ - $M_{\star}$ plot for the three cases of angular momenta are also investigated (Figure 1). However, because of the compactness of the simulated galaxies and since the radial distance of 2 kpc is noticeably larger than the scale of R_{eff} in Cadiou et al. (2022) for each simulation, the core density $\Sigma_{\star,1.2\text{kpc}}$ is selected.

3.2 Proper centering

As previously mentioned in Section 2, redefining the centres of the regions used to estimate the core density $\Sigma_{\star,1.2kpc}$ is necessary. The shrinking technique is incorporated into the analysis, and a new centre for each output is considered. Hence, it is rather important to confirm and monitor the accuracy of these new central points throughout the research procedure. For this reason, the particle plots for all given outputs are generated and examined for the four different simulated galaxies (reference, $\times 0.66$, $\times 1.2$, $\times 1.5$ cases). A total of 78 particle plots are produced and documented (39 centring on the dark matter and 39 centring on stars), and it is deduced that the new centres are very accurate after the implementation of the shrinking sphere method. A characteristic example where the distinction between the initial and the new centre is distinguishable is depicted in Figure 2.2 for the $\times 0.66$ simulation at $z = 2.5$. In both cases, the corresponding centres are annotated in red cross symbols (+) along with a circle representing the spherical region that encloses 20% of the galaxy that is used for the calculation of the core densities. Performing a visual comparison, it is observed that the difference between the corresponding central points, old and new, exceeds 25 kpc in the z axis.

The difference between the two centring methods is also visible in Figure 3.3 when pro-
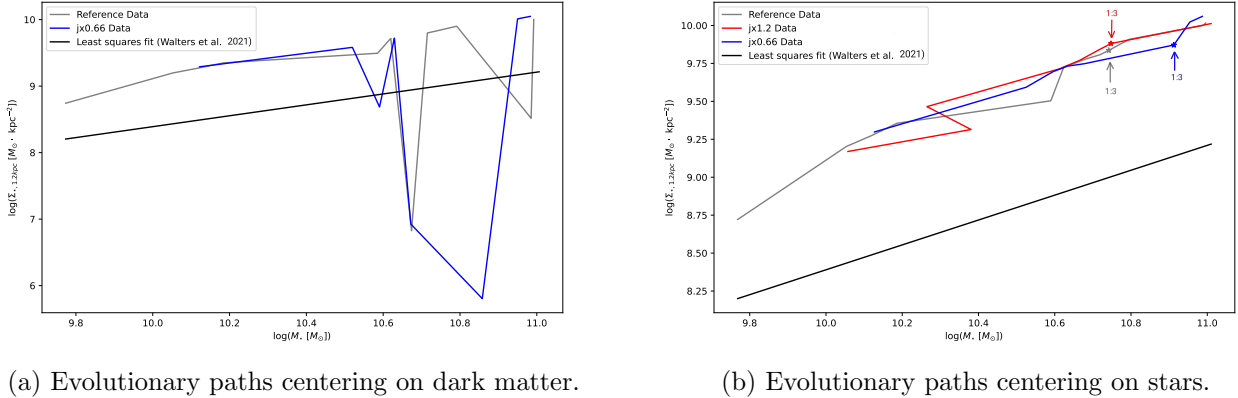
(a) Evolutionary paths centering on dark matter.   (b) Evolutionary paths centering on stars.

Figure 3.3: Comparison of the evolutionary tracks between the initial method (left) for the reference and the ×0.66 case of angular momentum and the analysis incorporating the shrinking sphere technique for all three simulations (right). At the first step of the process, the central surface density of the galaxy is determined using the old centres, which are estimated considering the dark matter of the halo. This method resulted in $\Sigma_{\star,1.2kpc}$ values with considerable offsets, as the definition of the centres is crucial when calculating the core density. The dips visible in sub-figure (a) represent the aforementioned offsets. When each centre is redefined by implementing the iterative method of the shrinking sphere, the discrepancy is eliminated. In sub-figure (b) the trajectories for the reference, the ×1.2, and the ×0.66 cases are depicted in different colours (grey, red, and blue respectively) no off-centred points are recorded. Also, outputs at which the satellites merged with the galaxy for each case are annotated by their stellar mass ratio (Cadiou et al. 2022).

ducing the $\Sigma_{\star,1.2\text{kpc}}$ - $M_\star$ plane. As stated in Chapter 2 the two spherical regions that are used to compute the core density $\Sigma_{\star,1.2\text{kpc}}$ are centred on dark matter particles only. As the choice of which particles to centre on is integral during the analysis, this results in significantly lower values of $\Sigma_{\star,1.2\text{kpc}}$ for certain redshifts. These offsets are depicted as dips in Figure 3.3 (a) for the reference and ×0.66 angular momentum scenarios. The inconsistencies originating from the centring technique occur for all four simulations but for our convenience, only two of these cases are plotted in Figure 3.3 (a). However, after redefining the centres relative to stellar particles and modifying the initial approach, the evolutionary trajectories of the simulated galaxies are created and as can be seen from Figure 3.3 (b) there exists no centring issue.

3.3 Evolutionary paths

W21 proposed that the angular momentum of the accreting gas has the ability to control the slope of the $\Sigma_{\star,r}$ - $M_\star$ plane. More precisely, a pattern that correlates the inclination of the evolutionary paths with the total specific angular momentum of galaxies is suggested;

low angular momentum galaxies have steeper slopes in $\Sigma_{\star,r}$ - $M_\star$, contrary to halos with higher values of angular momentum that exhibit shallower slopes. To determine if angular momentum is the reason behind this trend, the coevolution over time of the stellar mass($M_\star$) and the core density ($\Sigma_{\star,1.2kpc}$) is analysed for the galaxies that $j_\star$ has been modified. As discussed in Chapter 2 the galactic history of halo A is studied for three different scenarios of angular momentum namely, the reference case, the $\times1.2$ case, and the $\times0.66$ case. In the reference instance, the galaxy is evolving naturally without any alternations regarding its angular momentum. In contrast, the cases $\times1.2$ and $\times0.66$ refer to the situations where $j_\star$ has been genetically modified from the reference case by the respective factors. The data utilised to trace the histories of these halos span from redshift $z = 3.7$ to $z = 1.95$. At $z = 2$ each galaxy underwent a merger event that contributed to fluctuations in the initial values of angular momentum.

It is significant to note the importance of redshift 2 throughout the conducted data analysis. To be more specific, there are mainly two reasons that denote the key role of this redshift value. The former lies in the fact that $z = 2$ signifies a specific epoch in cosmic timescale when the star formation in galaxies was more efficient. Redshift 2 (which corresponds to 3 Gyr from the Big Bang) is the appropriate epoch where observations can be made with significant ease while simultaneously being affordable compared to lower z such as $z = 0$ (13.7 Gyr from the Big Bang), which is four times more expensive (Roca-Fàbrega et al. 2024) The latter and most important one is that any difference in the slope of the $\Sigma_{\star,1.2kpc}$ - $M_\star$ plane is expected to be visible close to or at $z = 1.95$. More concretely, the modification of the early Universe conditions that led to the alternation of initial angular momentum of the baryons took place when the satellite merged with the galaxy at redshift 2. In other words, $j_\star$ of the satellite deviates from its original value in the reference case, and thus the merger acts as a catalyst that leads to the different cases of $j_\star$. Hence, the dominant angular momentum, which influences the whole system and eventually leads to three distinct galaxies, originates from the merger and goes to the outskirts of the halo. Prior to this event, the galaxy in all different scenarios is evolving similarly.

In Figure 3.4 the evolutionary paths of halo A for the three distinct cases (reference, $\times1.2$, $\times0.66$) can be seen, tracing their histories from $z = 3.7$ to $z = 1.95$. The process that is followed to create such a diagram consists of three steps that are going to be thoroughly explained. First and foremost, the mass of the stellar particles enclosed in the specified regions is calculated as described in Chapter 2. Then, utilising equation 2.1 the core density is computed for a fixed radius of 1.2 kpc. Converting these quantities into the relevant units ($M_\odot$ for $M_\star$ and kpc for r)is an integral part of this procedure, to ensure that the central surface density $\Sigma_{\star,1.2\mathrm{kpc}}$ is per $M_\odot \cdot kpc^{-2}$. For our convenience, the relevant obtained logarithmic $M_\star$ and $\Sigma_{\star,1.2\mathrm{kpc}}$ values are plotted against each other. Also, to achieve visual coherency, the resulting evolutionary trajectories are uniquely coloured according to their angular momentum values; grey for the reference case, blue for the x0.66 case, and red for the $\times1.2$ case. The solid line represents the least squares fit incorporating face-on data points for $\Sigma_{\star,1.2\mathrm{kpc}}$, i.e. $\log(\Sigma_{\star,1.2\mathrm{kpc}}) = 0.82(\log(M_\star) - 10.5) + 8.80$ (W21).

Before proceeding in the creation of the $\Sigma_{\star,1.2\mathrm{kpc}}$ - $M_\star$ plots, the obtained values for $\Sigma_{\star,1.2\mathrm{kpc}}$ and $M_\star$ are cross-referenced with the corresponding tabulated ones. In more detail, the mass of the stellar particles enclosed within the virial radius $M_\star(< R_{\mathrm{vir}})$ is in the order of $10^{11}\ M_\odot$, a result that is in agreement with both Cadiou et al. (2022) and W21. Regarding the documented $\Sigma_{\star,1.2\mathrm{kpc}}$ data it is noticed that there exists an increase compared to W21. Nevertheless, this is a rational outcome since the simulated galaxies are more compact than Illustris TNG as was previously discussed and thus exhibit denser cores.

The final step is distinguishing the exact output at which the satellites merged in the galaxies. The strategy implemented to perceive the epoch at which the merger events occurred is via the constructed particle plots. More concretely, through the particle plots generated for each provided snapshot of the galaxies, the ensemble of additional particles included in the satellite are visually recognised and thus the mergers are distinguished. As discussed before, it is expected to identify the last major mergers close to $z = 2$. In Figure 3.4 the outputs at which the secondary galaxies have merged are denoted.

An alternative way to document and archive galaxy mergers in large-scale simulations is via merger trees. In brief, possible merger events are identified usually by using the proximity between galaxies and their velocity in phase space. Subsequently, galaxies are recorded in a hierarchical order interconnecting progenitors and descendant galaxies for each output of the simulation (Tweed et al. 2009). However, for this analysis, the construction of merger trees is not needed as it is already known that the timing of the last main mergers is close to $z = 2$. Also, it is understood that a considerable amount of time is required to generate such diagrams since they include continuous and dynamical procedures that is not feasible for the duration of this study. In either case, both methods to find the major mergers, i.e. visual identification through particle plots or the creation of merger trees, provide the same result in this project's circumstances.

The main merger events are characterised by satellites with a mass ratio exceeding 1:8. Accordingly, halo A lacks any major satellite inside R_{vir} until redshift 2. This is true for the three different simulations that are studied, i.e. the reference, $\times 1.2$, and $\times 0.66$ cases. In Figure 3.4 the three merger events that have a mass ratio of 1:3 are annotated. As explained before, satellites act as catalysts for the modification of the stellar angular momentum in the simulations. When the major satellites fall through the virial radius of the central galaxy, $j_\star$ undergoes changes depending on the alignment and the orbit of the satellite (Cadiou et al. 2022). Following the completion of these mergers, the galactic stellar mass and angular momentum are primarily governed by the main galaxy's disk. As it will be discussed further down, the case where the angular momentum is altered by a factor of 1.5 undergoes a more notable merger of 1:2. Due to heightened $j_\star$, this merger event is postponed after redshift 2.00 (Cadiou et al. 2022).
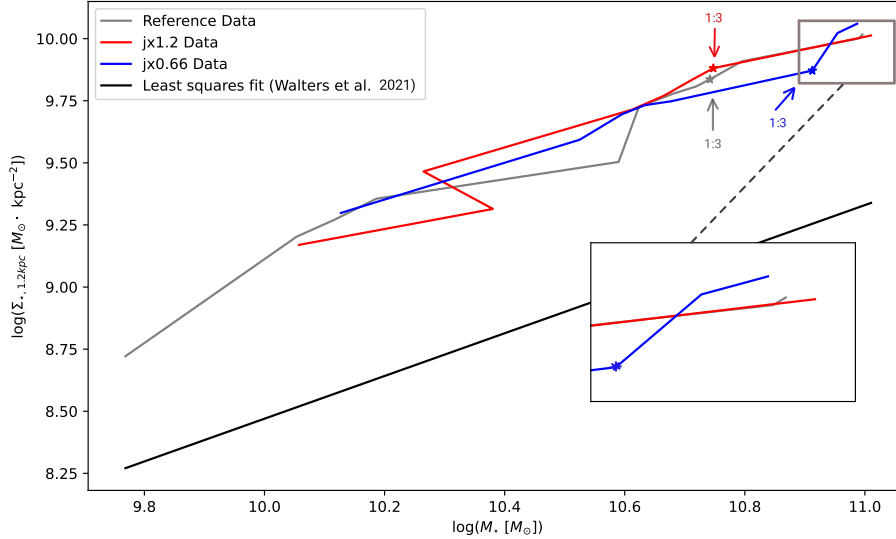
Figure 3.4: The evolutionary tracks of the halo A (Cadiou et al. 2022) for the three cases of angular momentum in the central stellar density $\log(\Sigma_{\star,1.2\mathrm{kpc}})$ against stellar mass $\log(M_\star)$ diagram. For ease of viewing, each trajectory has been coloured differently with the grey corresponding to the reference case, the blue to the $\times 0.66$ case and the red to the $\times 1.2$ case of angular momentum. The black line is the least squares fit for all three galaxies using face-on values for the stellar mass surface density $\Sigma_{\star,1.2\mathrm{kpc}}$ (W21). The time for which the secondary galaxies are within the virial radius and consequently merge is illustrated for each case with the relevant coloured arrows. Additionally, the ratio of each satellite's stellar mass with respect to the $M_\star$ of the galaxy (Cadiou et al. 2022) is also annotated.

3.4 Comparison with W21

Following the previous analysis, the track history of the halos in the $\Sigma_{\star,1.2\mathrm{kpc}}$ - $M_\star$ plane are generated. The creation of these paths will allow for a comparison with the emergent trend stated in W21 to be made and hence understand if angular momentum is the driving force behind it. Two observations can be noted from Figure 3.4. Firstly, documenting the $\Sigma_{\star,1.2\mathrm{kpc}}$ values for the three halos, it holds that the simulated galaxies are rather compact and hence core densities are at the higher end of the spectrum. This remark is confirmed from the corresponding plots in W21 where it can be seen that galaxies of the Illustris TNG simulation with denser cores developed an abrupt augmentation in their tracks compared to those with diffuse cores.

The second result (and one of the most important ones), is that there is an indication of a possible pattern regarding the influence of angular momentum in the $\Sigma_{\star,1.2\mathrm{kpc}}$ - $M_\star$ plane at the last two outputs, which can be seen from the zoomed-in part of Figure 3.4.

More concretely, comparing the slopes of the three plotted tracks, it can be distinguished that the trajectory corresponding to the galaxy scenario with a scaling factor of 0.66 has a steeper slope. Also, the ×1.2 simulation has an inclination with minimal fluctuations. The reference galaxy develops in a similar fashion to the ×1.2 scenario, but a slight implication that might progress by increasing its slope compared to the ×1.2 case exists towards the end of the simulation. Furthermore, it is shown that the trajectories of the three galaxies diverge towards the end of the simulation namely, at redshifts 2 and 1.95. This is a rational observation as the alternations in angular momentum occurred after the satellites merged with the galaxies and hence the timing at which the last major merger happened is when it is expected for any trend to start emerging. As mentioned above, before the merger events, all three galaxies evolved similarly without any external influence on their $j_\star$.

It is noted that by no means a distinct pattern is found and hence a direct comparison with W21 is not possible. However, there are some hints about a possible emergence of the predicted pattern that if confirmed would indicate that the galactic paths in $\Sigma_{\star,1.2\mathrm{kpc}}$ - $M_\star$ are driven by the angular momentum. Consequently, it is clear that to record such a clear pattern between the slopes the simulations would need to run for a longer time namely, for $z < 1.95$. In doing so, galaxies will have the opportunity to evolve for several Myr, contributing supplementary data. Ideally, the correlation between the three paths will be that the galaxy with the lowest angular momentum will have the steepest slope and the halo with the highest value of $j_\star$ will develop with considerably less slope increase. The Illustris TNG simulation progresses until $z = 0$ and hence has enough time for a pattern to develop.

Another interesting remark is the correlation between the surface density profile (Figure 3.1) and the tracks that trace the histories of each galaxy. To be more specific, the density profile showed that the curves of each halo are closely located to each other, apart from small deviations at specific radial intervals, that they are practically indistinguishable. This behaviour is also identified in the $\Sigma_{\star,1.2\mathrm{kpc}}$ - $M_\star$ plane. In Figure 3.4 it can be seen that the evolutionary tracks have complex behaviour throughout their evolution and that the differences between the trajectories for each halo are minimal. This tendency to very small deviations between the evolutionary tracks of the simulations persists even when the core density $\Sigma_{\star,N}$ is plotted against $M_\star$ for several different r values except the chosen 1.2 kpc. The cases of $\Sigma_{\star,0.1\mathrm{kpc}}$, $\Sigma_{\star,0.2\mathrm{kpc}}$, $\Sigma_{\star,0.3\mathrm{kpc}}$, $\Sigma_{\star,0.4\mathrm{kpc}}$, $\Sigma_{\star,0.5\mathrm{kpc}}$, $\Sigma_{\star,1.5\mathrm{kpc}}$, and $\Sigma_{\star,2\mathrm{kpc}}$ (Figure 1) are also examined and each plot illustrated the minor divergences between the tracks. This is a notable and worth-mentioning outcome as it implies that dramatic changes in the history of the galaxies influence the central galactic regions to a very small degree until $z = 1.95$.

Lastly, the case where $j_\star$ is modified by a factor of 1.5 with respect to the reference galaxy is also studied. A similar procedure is followed to construct the evolutionary path of the ×1.5 case in the $\log(\Sigma_{\star,1.2kpc})$ - $\log(M_\star)$ diagram, as is illustrated in Figure 3.5. Yet, the latter case is omitted from our investigation as the central galaxy within halo A is characterised by a non-equilibrium state and experiences a notable merger event with a mass
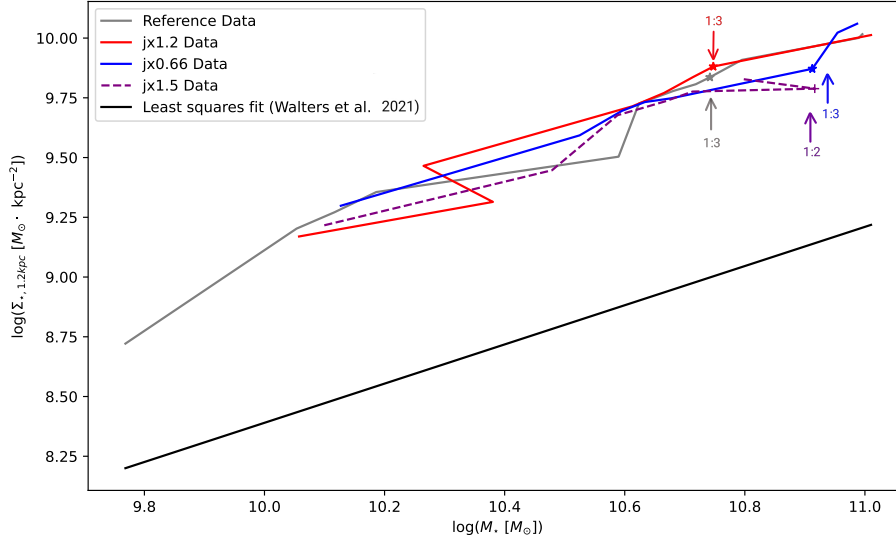
Figure 3.5: Plot illustrating the progressive paths for four different scenarios of angular momentum; the reference case, the x1.2 case, the x0.66 case, and the x1.5 case denoted as grey, red, blue, and dashed purple curves.

ratio of 1:2 (Cadiou et al. 2022). The satellite reaches its apocenter, i.e. the farthest point in its orbital trajectory (Li et al. 2021), from the main galaxy at $z = 2$, which leads to a notable displacement regarding the galactic system's centre of mass and the main galaxy's centre (Cadiou et al. 2022). The pericenter which marks the closest point between the orbit of the satellite and the galaxy (Li et al. 2021) happens at $z = 2.06$ (Cadiou et al. 2022). From this sequence of motions, it can be deduced that the merger occurred at a later z than the other angular momentum cases after the satellite had concluded its orbit.

Chapter 4

Conclusions and Discussion

In conclusion, the goal of this project is to examine the coevolution of the core density $\Sigma_{\star,1.2\text{kpc}}$, a quantity that represents the compactness of a galactic system, and the stellar mass $M_\star$ for simulated galaxies, and particularly investigate if the development of the galaxies in the $\Sigma_{\star,1.2\text{kpc}}$ - $M_\star$ plot is driven by the angular momentum. This is achieved by testing the accuracy of the suggested trend regarding the slope of the evolutionary tracks in the Illustris TNG simulation, i.e. subhalos with low angular momentum have comparably steeper slopes than galaxies with high angular momentum (W21). The trajectories in the $\Sigma_{\star,1.2\text{kpc}}$ - $M_\star$ plane of three simulations where the angular momentum has been altered are produced and compared with the proposed pattern in W21. The three simulated halos that are thoroughly investigated consist of a reference galaxy and two additional cases where the reference galaxy is resimulated with two different values of angular momenta ($\times 1.2$, $\times 0.66$ cases).

Firstly, the fundamental mechanism behind the relevant simulations is comprehended, emphasising the role of satellites in transferring angular momentum. The initial cosmological conditions of the galaxies are genetically modified, which in turn postpones or rushes a major merger close to redshift 2. This leads to either an increase or decrease of the stellar angular momentum at $z = 2$. Creating the total stellar mass profiles also contributes to our understanding as all the aforementioned processes are depicted. The fixed radius of the central stellar density is selected to be $r = 1.2$ kpc, considering the slightly more compact morphology of the galaxies (compared to observations) and the effective radii of each halo. The compact nature of the galaxies is a result of the choice of the simulation model that they are produced from and also the fact that at $z = 2$ galaxies are more compact than in lower redshifts (Swinbank et al. 2017). The Illustris TNG simulation runs until $z = 0$ and hence the choice of a $r < 2$ kpc is one of the main differences between W21 and this project.

The next step is to compute $\Sigma_{\star,1.2\text{kpc}}$ - $M_\star$ incorporating into our method the shrinking sphere iterative technique. Choosing to centre on stellar particles instead of dark matter plays a crucial role during the analysis since it ensures that $\Sigma_{\star,1.2\text{kpc}}$ is properly centred, as confirmed by the corresponding particle plots. After establishing the proper centres, the

evolutionary trajectories of the three galaxies are generated. In the $\Sigma_{\star,1.2\text{kpc}}$ - $M_\star$ diagram, the investigation about the emergence of a possible pattern between the plotted paths is focused towards the final output of the simulation, as it is expected to occur close to $z = 2$ due to the timing of the last major merger. Interpreting our results, it is still unclear if the angular momentum can predict how steep the galactic trajectories would be as there exist some hints about the emergence of the expected pattern. The three simulations start diverging towards the end of the simulation and hence the duration of simulations needs to be extended. Given enough time, it is hypothesised that a more clear pattern will be observed at $z < 1.95$. We also note that the Illustris TNG simulation in W21 runs for lower redshift values i.e. $z = 0$.

Moreover, some intriguing conclusions can be made from the interpretation of the surface density profile for the three galaxies at $z = 1.95$. In more detail, the resulting curves in the created profile are indistinguishable from each other providing no additional information regarding the choice of r in $\Sigma_{\star,r}$ contrary to what was expected. This behaviour is also reflected in the $\Sigma_{\star,1.2\text{kpc}}$ - $M_\star$ plane as the difference between the evolutionary paths of the simulations is minimal. This is a very interesting result of the analysis as it indicates that despite the significant differences in the history of the halos, the core regions of the galaxies respond in a very similar way. This observation is thus of particular interest for constraining the formation scenarios concerning bulges and related structures.

In general, stellar angular momentum correlates with Hubble morphology. Several studies are dedicated to investigate the mechanisms behind the distribution of angular momentum and what impact it can have in the galactic structure. Romanowsky & Fall (2012) suggests that all types of galaxies consist of two different components; a bulge and a disk. Each of these galactic parts is characterised by a different reservoir of stellar angular momentum and hence the morphology can be interpreted as a combination of high and low $j_\star$ material. Depending on the balance between these different values of $j_\star$, the galaxy may possess a more dominant bulge or disk structure.

Data from the reference case of halo A and the galaxies with the three different $j_\star$ cases ($\times 1.2$, $\times 0.8$, $\times 0.66$) have tested how angular momentum can influence the galactic morphology. If the stellar mass of a galaxy is kept unchanged, then the morphological characteristics of the galaxy are influenced by alternation in $j_\star$. More precisely, for high values of $j_\star$ ($\times 1.2$ case), the halo demonstrates a ring-like structure with a notable galactic disk. The galaxy's spatial distribution extends over a large area and a minimal bulge exists. However, for simulations with low angular momentum ($\times 0.66$ case), the halo is comparably more compact exhibiting a noticeable bulge part with a less definite disk (Cadiou et al. 2022). If the proposed trend in W21 is confirmed, then knowing the angular momentum of a halo could provide indications of what type of galaxy it will evolve to be i.e. with a more prominent bulge or spatially extended with a disk.

Therefore, galaxies with low angular momentum and steeper slopes in the $\Sigma_{\star,1.2\text{kpc}}$ - $M_\star$

plane, will have a more compact morphology with a notable bulge. In contrast, galaxies with shallower inclination in their evolutionary trajectories will be more expanded in space and will have a more significant disk and ring-like structure. As mentioned in Chapter 1, the way simulations can contribute to our understanding of why there exist these two distinct morphologically diverse galaxies is a very broad and complex question, that this partially addressed in this project. In any case, the size of the provided simulations needs to be increased and extended to lower redshifts ($z < 1.95$).

To summarise, there are three key results in this project. First, the compactness of the simulations influenced a lot the data analysis, especially regarding the selection of a fixed radial distance r that is chosen to be 1.2 kpc. It also resulted in slightly increased values of core density. The evolutionary trajectories that trace the histories of the three galaxies are successfully generated, however, the expected trend between their slopes is not clearly identified. Instead, there exist some hints regarding the emergence of the proposed pattern close to $z = 2$. Therefore, supplementary data for lower redshift values need to be included. Moreover, the surface density profiles at $z = 1.95$ showed that despite the alterations made in the halo history, the core of the galaxies behaves in a similar fashion.

Lastly, an additional suggestion for future improvement is to focus the data analysis on young stars. It is true that the outermost regions of the galaxies consist of younger stars and that the core of the galaxies is comprised of older stars (Woo & Ellison 2019; Walters et al. 2021). Young stars encode more strongly the recent history of the three galaxies when their total angular momentum has started diverging. Hence, incorporating an age requirement for the stars to be younger in the method could potentially result in a stronger trend.

Bibliography

Aarseth, S. J. 2003, Gravitational N-Body Simulations

Bernardini, M., Mayer, L., Reed, D., & Feldmann, R. 2020, MNRAS, 496, 5116

Cadiou, C., Pontzen, A., & Peiris, H. V. 2021, MNRAS, 502, 5480

Cadiou, C., Pontzen, A., & Peiris, H. V. 2022, MNRAS, 517, 3459

Carroll, B. W. & Ostlie, D. A. 1996, An Introduction to Modern Astrophysics

Dubois, Y., Beckmann, R., Bournaud, F., et al. 2021, A&A, 651, A109

Forbes, J. C., Krumholz, M. R., Burkert, A., & Dekel, A. 2014, MNRAS, 438, 1552

Hogg, D. W. 1999, arXiv e-prints, astro

Hunter, J. D. 2007, Computing In Science & Engineering, 9, 90

Kepner, J. V. 1999, ApJ, 520, 59

Kluyver, T., Ragan-Kelley, B., Pérez, F., et al. 2016, in Positioning and Power in Academic Publishing: Players, Agents and Agendas, ed. F. Loizides & B. Schmidt, IOS Press, 87 – 90

Kroupa, P. 2001, MNRAS, 322, 231

Li, H., Hammer, F., Babusiaux, C., et al. 2021, ApJ, 916, 8

Mancera Piña, P. E., Posti, L., Fraternali, F., Adams, E. A. K., & Oosterloo, T. 2021, A&A, 647, A76

Matsumoto, T. 2024, ApJ, 964, 133

Power, C., Navarro, J. F., Jenkins, A., et al. 2003, MNRAS, 338, 14

Roca-Fàbrega, S., Kim, J.-h., Primack, J. R., et al. 2024, arXiv e-prints, arXiv:2402.06202

Romanowsky, A. J. & Fall, S. M. 2012, , 203, 17

Roth, N., Pontzen, A., & Peiris, H. V. 2016, MNRAS, 455, 974

Sellwood, J. A. 2014, Reviews of Modern Physics, 86, 1

Stopyra, S., Pontzen, A., Peiris, H., Roth, N., & Rey, M. P. 2021, , 252, 28

Suto, D., Kitayama, T., Osato, K., Sasaki, S., & Suto, Y. 2016, , 68, 14

Swinbank, A. M., Harrison, C. M., Trayford, J., et al. 2017, MNRAS, 467, 3140

Teklu, A. F., Remus, R.-S., Dolag, K., et al. 2015, ApJ, 812, 29

Teyssier, R. 2002, A&A, 385, 337

Turk, M. J., Smith, B. D., Oishi, J. S., et al. 2011, The Astrophysical Journal Supplement Series, 192, 9

Tweed, D., Devriendt, J., Blaizot, J., Colombi, S., & Slyz, A. 2009, A&A, 506, 647

Walters, D., Woo, J., Ellison, S. L., & Hani, M. H. 2021, MNRAS, 504, 1677

Wes McKinney. 2010, in Proceedings of the 9th Python in Science Conference, ed. Stéfan van der Walt & Jarrod Millman, 56 – 61

White, S. D. M. 1984, ApJ, 286, 38

Woo, J. & Ellison, S. L. 2019, MNRAS, 487, 1927

Zolotov, A., Dekel, A., Mandelker, N., et al. 2015, MNRAS, 450, 2327

Appendix

The code describing the shrinking sphere method (Power et al. 2003) is as follows:

```python
def shrinking_sphere(ds,center,radius,*,center_on="star",
        shrink_factor=0.95,):

    if isinstance(radius, tuple):
        radius = ds.quan(*radius).to("code_length")
    if isinstance(center, tuple):
        center = ds.arr(*center)
    sp0 = ds.sphere(center, radius)

    pos = sp0[center_on, "particle_position"].to("code_length")
    m = sp0[center_on, "particle_mass"][:, None].value
    center_0 = center.copy()

    while len(pos) > 1000:
        yt.mylog.debug("Shrinking sphere radius:
        dx: %s kpc/h\tnpart: %8d"%((center - center_0).to("kpc/h").value,len(pos),))
        r = np.linalg.norm(pos - center, axis=1)
        order = np.argsort(r)

        # Retain the x% closest to the center
        new_len = min(int(len(pos) * shrink_factor), len(pos) - 1)
        pos = pos[order][:new_len]
        m = m[order][:new_len]

        # Compute new center of mass
        center = np.sum((pos * m), axis=0) / m.sum()

    return center
```
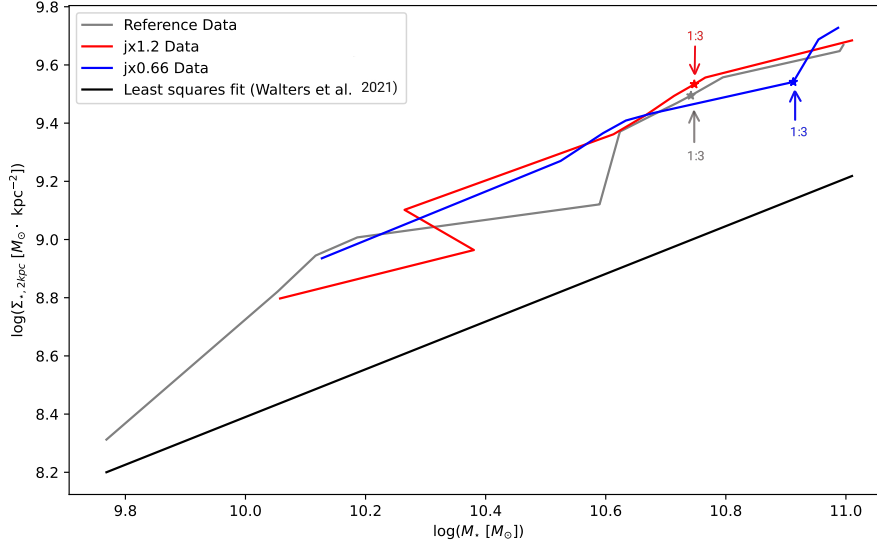
Figure 1: $\Sigma_{\star,2\text{kpc}}$ - $M_\star$ plot tracing the histories of the three galaxies (reference, $\times 1.2$, $\times 0.66$ cases) for a core density of fixed radius $r = 2$ kpc. The solid line is the least squares of the three galaxies feat for the core density $\Sigma_{\star,2\text{kpc}}$ (W21). The main merger events with mass ration 1:3 (Cadiou et al. 2022) that occurred towards the end of the simulation are annotated for visual reference.

Table 1: Table containing the logarithmic values for $\Sigma_{\star,R_{\text{eff}}}$ for halo A for the three cases of $j_\star$ at redshift 1.95. These values are computed from the given stellar mass and effective radius in Cadiou et al. (2022) and are used to qualitatively evaluate our results. The units for the central surface density are $[M_\odot \cdot kpc^{-2}]$.

$j_\star$ case	$\log(\Sigma_{\star,R_{eff}})$
x0.66	10.3
Reference	10.1
x1.2	9.99

Table 2: Table consisting of the calculated half mass radii $R_{1/2}$ for the three simulated galaxies (reference, $\times 1.2$, $\times 0.66$ cases) at redshift 1.95. These radial values are estimated from the stellar mass profiles and are used to cross-reference our results.

$j_\star$ case	$R_{1/2}$ [kpc]
$\times 0.66$	1.08
Reference	1.81
$\times 1.2$	2.13